WiDetect: Robust Motion Detection with a Statistical Electromagnetic Model

FENG ZHANG, University of Maryland, College Park and Origin Wireless, Inc.
CHENSHU WU, University of Maryland, College Park and Origin Wireless, Inc.
BEIBEI WANG, University of Maryland, College Park and Origin Wireless, Inc.
HUNG-QUOC LAI, Origin Wireless, Inc.
YI HAN, Origin Wireless, Inc.
K. J. RAY LIU, University of Maryland, College Park and Origin Wireless, Inc.

Motion detection acts as a key component for a range of applications such as home security, occupancy and activity monitoring, retail analytics, etc. Most existing solutions, however, require special installation and calibration and suffer from frequent false alarms with very limited coverage. In this paper, we propose WiDetect, a highly accurate, robust, and calibration-free wireless motion detector that achieves almost zero false alarm rate and large through-the-wall coverage. Different from previous approaches that either extract data-driven features or assume a few reflection multipaths, we model the problem from a perspective of statistical electromagnetic (EM) by accounting for all multipaths indoors. By exploiting the statistical theory of EM waves, we establish a connection between the autocorrelation function of the physical layer channel state information (CSI) and target motion in the environment. On this basis, we devise a novel motion statistic that is independent of environment, location, orientation, and subjects, and then perform a hypothesis testing for motion detection. By harnessing abundant multipaths indoors, WiDetect can detect arbitrary motion, be it in Line-Of-Sight vicinity or behind multiple walls, providing sufficient whole-home coverage for typical apartments and houses using a single link on commodity WiFi. We conduct extensive experiments in a typical office, an apartment, and a single house with different users for an overall period of more than 5 weeks. The results show that WiDetect achieves a remarkable detection accuracy of 99.68% with a zero false rate, significantly outperforming the state-of-the-art solutions and setting up the stage for ubiquitous motion sensing in practice.

CCS Concepts: • **Human-centered computing → Ubiquitous and mobile computing**;

Additional Key Words and Phrases: WiFi sensing, Motion detection, Statistical EM wave theory

ACM Reference Format:
Feng Zhang, Chenshu Wu, Beibei Wang, Hung-Quoc Lai, Yi Han, and K. J. Ray Liu. 2019. WiDetect: Robust Motion Detection with a Statistical Electromagnetic Model. *Proc. ACM Interact. Mob. Wearable Ubiquitous Technol.* 3, 3, Article 122 (September 2019), 24 pages. https://doi.org/10.1145/3351280

Authors' addresses: Feng Zhang, University of Maryland, College Park and Origin Wireless, Inc. feng.zhang@originwireless.net; Chenshu Wu, University of Maryland, College Park and Origin Wireless, Inc. cswu@umd.edu; Beibei Wang, University of Maryland, College Park and Origin Wireless, Inc. bebewang@umd.edu; Hung-Quoc Lai, Origin Wireless, Inc. quoc.lai@originwireless.net; Yi Han, Origin Wireless, Inc. yi.han@originwireless.net; K. J. Ray Liu, University of Maryland, College Park and Origin Wireless, Inc. kjrliu@umd.edu.

2474-9567/2019/9-ART122 $15.00
https://doi.org/10.1145/3351280

Table 1. Comparison among different technologies.

	Camera	PIR	Pressure	Sound	WiFi-based	
					Existing	WiDetect
Accurate	✗	✗	✓	✓	✓	✓
Robust	✗	✓	✓	✗	✗	✓
Coverage	LOS	LOS	Contact	Room	Room	Whole home
Calibration-free	✓	✓	✓	✓	✗	✓

1 INTRODUCTION

Motion detection plays a fundamental role in many applications such as security surveillance, intruder detection, in-home occupancy and activity monitoring, smart building analytics, in-car child presence detection, etc. A key to motion detection is a ubiquitous and inexpensive motion sensor that should ideally satisfy the following three requirements, in addition to very high accuracy (i.e., detection rate):

- **Robust**: It should be robust and reliable, ideally producing (approximately) zero false alarms.
- **Large coverage**: It should work for a large area without a dense placement of many sensors. Specifically, a single sensor should be able to sense motions not only within a close Line-Of-Sight vicinity but also behind multiple walls.
- **Calibration-free**: It should be independent of environments, locations, orientations, and subjects, and should not require any kind of a priori calibration or training.

If the above requirements are satisfied, we could imagine motion sensing becoming a ubiquitous service with which, for example, a smart-home can intelligently respond to users with light and air conditioner, a smart digital assistant like Alexa and Google Home can actively interact with an approaching user before he needs to talk, and a smart car can detect and thus protect a child when it is forgotten in car unknowingly by parents.

However, to the best of our knowledge, no existing motion sensing technology satisfies all the above requirements (See Table 1). Existing approaches based on cameras, infrared, pressure and audio sensors not only require specialized hardware but also suffer from major drawbacks that prevent them from ubiquitous adoption. Video-based methods dominate the current market with a number of commercial products like Foscam, Dropcam, and Nest Cam, etc. Cameras, however, are vulnerable to non-motion environmental changes (e.g., sunlight condition, air flow close to heating or cooling vents), resulting in frequent false alarms. In addition, they cover only limited Line-Of-Sight (LOS) areas. To achieve larger coverage, multiple devices need to be installed at different locations. Moreover, video-based approaches raise significant privacy concerns and are unfavorable to many users. Infrared and indoor radars only support LOS motion sensing. Pressure sensors require contact, while sound sensors fail to detect silent motions.

Recently, WiFi has been considered as a promising solution for motion detection, which naturally circumvents shortcomings such as directive coverage and privacy intrusiveness that are inherent in previous technologies. The rationale is that radio signals are highly sensitive to the environmental perturbations, and thus environmental changes due to human movements can be captured by the dynamics of the channel state information (CSI) or the received signal strength indicator (RSSI). Most of the existing approaches then attempt to extract appropriate features from CSI/RSSI measurements for motion detection [23–25, 27, 31]. Despite the complicated detection methods, these approaches, however, have considerable limitations (See Table 2): First, they provide only limited coverage (typically LOS areas), although radio signals can penetrate walls. Extending the coverage immediately degrades their performance due to significant measurement noises in CSI, and thus multiple pairs of devices are required to cover a typical single house; Second, they often employ learning-based methods, which requires prior training to capture scenario-tailored parameters as well as recalibration over time to adapt to environmental

Table 2. A brief summary of different WiFi-based approaches.

Reference	Method	Claimed FN/FP	Calibration-free
RASID [10]	Estimate CDF of RSSI for normal state	4.7%/3.8%	✗
PILOT [25]	Variance of correlation (Radio map)	10.0%/10.0%	✗
E-eyes [22]	Match with CSI database (histogram/pattern)	10.0%/1.0%	✗
Omni-PHD [32]	Match with the histograms of the CSI	8.0%/7.0%	✗
DeMan [23]	SVD of CSI correlation matrix	5.9%/1.5%	✗
CARM [20]	Var. of the 2nd eig. of CSI correlation matrix	2.0%/1.4 per hour	✗
SIED [12]	Var. of the var. of CSI amplitudes	6.4%/2.0%	✗
FreeSense [27]	Phase diff. between the CSI waveforms	1.4%/0.5%	✗
WiDetect	**ACF of the power responses of CSI**	**0.3%/0.0%**	✓

* The results of prior works are mainly reported based on experiments over small area (e.g., a room) or relatively larger areas but with multiple links and within short periods (e.g., the same day). Instead, our results are evaluated from real-world deployment for over 5 weeks in whole apartment and house.

dynamics during long-term deployment; Third, since the CSI extracted from commodity WiFi devices is very noisy, they produce high false alarm rates and low detection rates that prevent their practical applications.

Based on the in-depth understanding of the physics of EM wave propagation, we find that the limited performance of previous works in realistic scenarios is mainly due to their unrealistic multipath models, which simplify signal propagation as mirror reflections and assume the existence of only one or several multipaths. Radio signals, however, scatter off reflectors and produce numerous multipath components in typical indoor environments [8], although some of them may be non-distinguishable by commercial CSI measurements. Previous efforts, e.g., [19] and [29], have been seeking for a geometric model for motion detection, which could only take several significant reflection paths into consideration. As a consequence, they lose the sensitivity for distant and micro motion, which is only captured by the multipath components that have traveled long distances, and thus fail to provide large coverage, while suffering from environmental noises.

In this work, we present the model, design, and implementation of WiDetect, the first motion detection system that achieves almost zero false alarms for whole-home coverage using only a single WiFi link. The key breakthrough lies in our investigation from a statistical perspective towards hundreds of scattering multipath components indoors. Although it is not possible to separate all multipath components indoors in the time domain due to insufficient bandwidth on commodity WiFi, we observe that, when a sufficiently large number of multipath components are involved, the statistical behaviors of the motion-induced CSI dynamics can be mathematically characterized by exploiting the statistical theory of electromagnetic waves [9]. Inspired by this, we build a statistical model that comprehensively leverages all existing multipath components for motion detection. To the best of our knowledge, we are the first to explore such statistical behaviors, rather than geometrical properties, of CSI for motion sensing. With this, WiDetect successfully turns a WiFi radio into an accurate and robust motion sensor that can be installed on pervasively existing WiFi infrastructure and made available to any device with a WiFi chip.

Specifically, we calculate the autocorrelation function (ACF) of the power response of the CSI and devise an efficient and effective motion statistic from the calculated ACF. Basically, the autocorrelation between consecutive CSI measurements will considerably increase in presence of motion, while remains at a low level around zero when there is no motion. Since our statistical model is independent of locations, environments and motion types, we are able to derive one general threshold for the motion statistic for different scenes, without any scenario-tailored training efforts. The relationship between the detection rate and false alarm rate for motion detection can also be theoretically derived. It can be shown that with a high channel sampling rate and a large

number of CSI samples, the false alarm rate can be almost zero, while a high detection rate and a large coverage are maintained. Unlike existing motion detection approaches that may not work well in extremely complicated environments with rich-scattering propagations, one unique feature of the proposed method is that it yields better performance with more multipath components.

To demonstrate WiDetect's performance, we have implemented WiDetect as a real-time system using two embedded devices equipped with commercial WiFi chipsets to set up a link between them. Our evaluation consists of three parts: 1) We conduct experiments in an office with about 240 m^2 to comprehensively study the factors that may impact WiDetect's performance. 2) We deploy WiDetect in a real-world smart-home monitoring application in a typical house with about 200 m^2 for over one week, which is equipped with 4 commercial passive infrared sensors (PIR). The evaluation results demonstrate that WiDetect achieves a true positive rate of 99.68% with a false positive rate as low as 0. As a comparison, the deployed commercial PIR-based security system only detects 86.80% of the motions due to LOS limitations. 3) WiDetect is installed in an apartment with the typical daily activity of two residents inside for up to one month. It turns out that the residents' lifestyle can be clearly monitored by the motion detection results of WiDetect. With remarkably high sensitivity and fairly low false alarms, we believe the proposed approach shapes a promising practical technology for ubiquitous device-free motion detection, allowing for a range of critical applications for a smart life.

To conclude, our core contributions are three folds:

(1) We build the first statistical model of radio signal propagation indoors that takes all scattering multipath components into consideration for motion detection, which is fundamentally different from previous geometrical models and underpins robust whole-home detection with a single link;
(2) We design an accurate and robust motion detector based on the proposed statistical model, which is independent of environments, locations, orientations, and subjects, and thus is generic to different scenarios without any training efforts;
(3) We implement a real-time system and deploy it at three different environments for a comprehensive evaluation and long-term study. Extensive experiments demonstrate WiDetect's superior performance for practical applications.

The rest of the paper is organized as follows. §2 summarizes the related works about the existing indoor motion detectors. §3 introduces the statistical modeling of CSI dynamics and §4 presents the basic principles, design, and implementation of WiDetect. Experimental evaluation is shown in §5 and §6 concludes the paper.

2 RELATED WORKS

Indoor Motion Detection: In general, the existing solutions for indoor motion detection can be classified into two categories: device-based and device-free.

Device-based solutions mainly utilize contact sensors, such as accelerometer and gyroscope [11, 13], to detect the movements of the human body. These approaches require users to either carry a smartphone or be equipped with wearable devices. Although the sensors can provide accurate and reliable information on people's activities and behaviors, they can also make people's lives more complicated and inconvenient. In addition, these methods are not suitable for applications like home security.

Device-free solutions are proposed to detect human motions without requiring people to carry any devices. Most of the existing solutions use camera [21], passive infrared (PIR) [28], audio [16] or RADAR [18] to monitor human activities. The camera-based and PIR-based systems suffer from limited directive coverage, and usually, multiple devices are needed for large areas and multiple rooms. The audio-based system [16] usually experience ambient noise and weak echo audio signal, which limits the sensing area greatly. RADAR-based systems usually do not work well for the indoor environment due to the multipath effect. Recently, several RADAR systems have been developed for indoor human motion detection and recognition, e.g., WiTrack [1] and WiSee [14]. However,

specialized and costly hardware, e.g., USRP [2], is required. In this work, we use commodity WiFi devices to detect human motion indoors.

WiFi-based Motion Detection: RASID [10] is an early system that exploits the fluctuations of WiFi signals to detect the presence of human beings in the environment. It first estimates the cumulative distribution function (CDF) of the receive signal strength indicator (RSSI) for a normal state (motion-free environment), and then detects motion by comparing the difference between the CDF of newly collected RSSI and the CDF of the normal state. Since CSI is a more detailed description of the channel responses, PILOT [25] decomposes the CSI amplitude correlation matrix using SVD and monitors the variations of the singular vectors continuously. Later on, various methods are proposed. Table 2 summarizes and compares these approaches. All of them need more or less calibration before use: some, e.g., E-eyes [22], CARM [20], TR-BREATH [5] and Omni-PHD [32], need to build a database storing the CSIs for the normal state and motion is detected as long as the incoming CSI is very dissimilar to the stored CSIs; others, e.g., DeMan [23], PADS [15], FreeSense [27], FreeDetector [34] and SIED [12], investigate intrinsic features of the CSI in the presence of human motion yet need a training phase to tune system parameters in order to balance the false positive rate and false negative rate. Basically, most of the existing works apply a data-driven approach and try to extract features from CSIs to distinguish between motion and non-motion scenarios. However, since the CSIs, extracted from commodity Wi-Fi devices, are very noisy and the stored CSIs under the non-motion scenarios are vulnerable to environmental changes, it is extremely hard to obtain stable features which are immune to environmental dynamics. As a result, most of the existing systems need to be calibrated or trained before in use. In addition, their performance (in terms of coverage, accuracy, and computation) is far from meeting the requirement of real applications, especially the very high false alarm rate. These drawbacks motivate us to propose a more robust, accurate and easy-to-use motion detector, which is demonstrated to be capable of achieving almost zero false alarm rate while maintaining a high detection rate over a very large area.

3 STATISTICAL MODELING OF CSI

In this section, we present our statistical modeling of CSI measured on commodity WiFi devices, which underly the foundation of accurate and robust whole-home motion sensing by comprehensively accounting for all possible multipaths indoors. We first introduce CSI, then analyze the measurement noises, and finally model the impacts of motion on CSI. We also verify the proposed model with primary experiments before we present the detailed design of WiDetect in the next section.

3.1 CSI with Motion

Consider a wireless link between a pair of WiFi devices, one as a transmitter (Tx) and the other as a receiver (Rx). Let $X(t, f)$ and $Y(t, f)$ be the transmitted and received signals over a subcarrier with frequency f at time t. Then, the CSI estimation for the subcarrier with frequency f measured at time t is $H(t, f) = \frac{Y(t,f)}{X(t,f)}$ [6], which is a complex number and can be obtained from the PHY layer of commercial WiFi. In practice, however, the measured $H(t, f)$ suffers from severe synchronization errors, including carrier frequency offset (CFO), sampling frequency offset (SFO), symbol timing offset (STO), and jitters of the phase-locked loops (PLLs), etc [26][4]. These errors significantly distort CSI phase, which can hardly be calibrated automatically in practice and thus prevent its practical usage [17, 20]. Fortunately, the impact on CSI amplitude is negligible. As a consequence, WiDetect only exploits the measured CSI amplitude for motion sensing.

Specifically, WiDetect employs the power response $G(t, f)$ of a CSI measurement $H(t, f)$, which is defined as the square of its magnitude and takes the form of

$$G(t, f) \triangleq |H(t, f)|^2 = \mu(t, f) + \varepsilon(t, f), \tag{1}$$

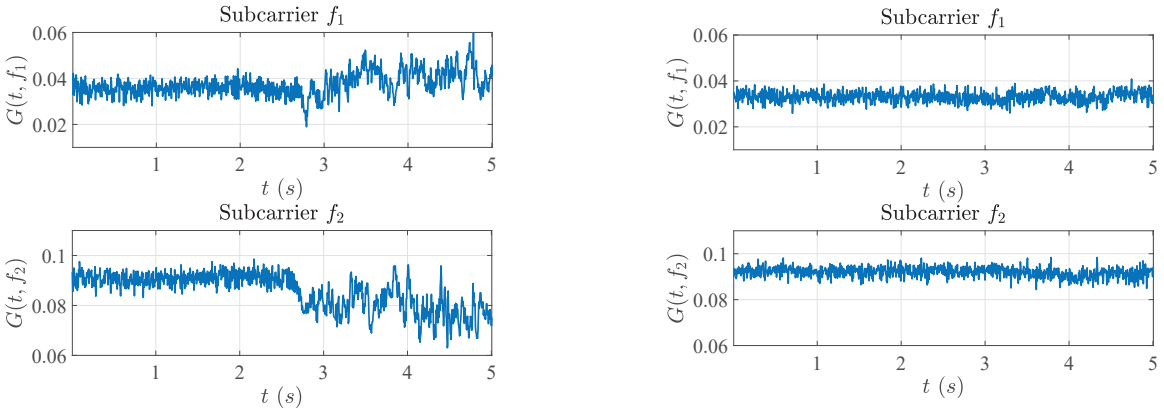

(a) Human motion in a nearby area.

(b) Human motion in a faraway area.

Fig. 1. Illustrations of the impact of human motion on the power response.

where $\mu(t, f)$ denotes the part contributed by the signal propagations, and $\varepsilon(t, f)$ denotes the measurement noise. Fig. 1 illustrates the impacts of human motion on the power responses measured by a pair of commodity WiFi devices. Several observations can be accordingly inferred as follows from the measurements.

(1) When the environment is static (i.e., motion free), $G(t, f)$ can be approximated as a constant value superimposed with an additive noise, i.e., $\mu(t, f)$ in (1) is assumed to be a constant;
(2) When the environment changes due to human motion, $G(t, f)$ can be approximated as a time-varying signal $\mu(t, f)$ superimposed with an additive noise;
(3) The changes of the magnitude of $\mu(t, f)$ is much larger when motion is closer to the link than when motion happens in a faraway area.
(4) The impacts of human motion on the power responses $G(t, f)$ of different subcarriers are different.

Based on these intuitive observations, we formally model the signal and noise terms in $G(t, f)$ and quantify the impacts of motion on the power response $G(t, f)$ in the following.

3.2 Modeling the Measurement Noise

In the following, the statistical properties of the measurement noise are analyzed. When the environment is static, the signal term $\mu(t, f)$ should be invariant in time since the physical paths that the EM waves undergo are unchanged and thus, the variation of $G(t, f)$ should be entirely caused by the measurement noise $\varepsilon(t, f)$.

We first conclude and validate two properties of the measurement noises:

Remark 1. *Given a subcarrier with frequency $f \in \mathcal{F}$, $\varepsilon(t, f)$ can be approximated as an additive white Gaussian noise with zero mean and a variance of $\sigma^2(f)$, i.e., $\varepsilon(t, f) \sim \mathcal{N}(0, \sigma^2(f))$.*

Remark 2. *The measurement noises $\varepsilon(t_1, f_1)$ and $\varepsilon(t_2, f_2)$ are independent for any two different subcarriers $f_1 \neq f_2$ or any two different time slots $t_1 \neq t_2$ when the CSI is measured.*

We validate this assumption via a set of one-hour CSI data collected in a static indoor environment.
(1) Normality: First, to verify the normality of the noise measured on each subcarrier, the quantile-quantile (Q-Q) plot of the normalized $G(t, f)$ and standard normal distribution for a given subcarrier is shown in Fig. 2a. As seen, the distribution of the noise is very close to a normal distribution.

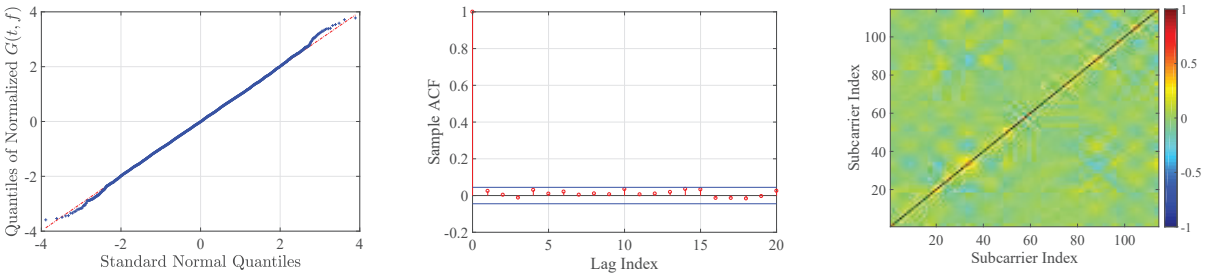

(a) Q-Q plot of noise. (b) Sample ACF of noise. (c) Cross-correlation matrix.

Fig. 2. Statistical behaviors of the noise.

(2) Whiteness: Second, to verify the whiteness of the noise, we study the ACF of $G(t,f)$ that can be defined as $\rho_G(\tau,f) = \frac{\gamma_G(\tau,f)}{\gamma_G(0,f)}$, where $\gamma_G(\tau,f)$ denotes the auto-covariance function, i.e., $\gamma_G(\tau,f) \triangleq \text{cov}(G(t,f), G(t-\tau,f))$ [3]. In practice, sample auto-covariance function $\hat{\gamma}_G(\tau,f)$ is used instead, which is defined as

$$\hat{\gamma}_G(\tau,f) = \frac{1}{T}\sum_{t=\tau+1}^{T}\left(G(t-\tau,f)-\bar{G}(f)\right)\left(G(t,f)-\bar{G}(f)\right), \tag{2}$$

where T is the number of samples and $\bar{G}(f) \triangleq \frac{1}{T}\sum_{t=1}^{T} G(t,f)$. If $\varepsilon(t,f)$ is white noise, the sample ACF $\hat{\rho}_G(\tau,f)$, for $\forall\tau \neq 0$, can be approximated by a normal random variable with zero mean and standard deviation $\sigma_{\hat{\rho_G}(\tau,f)} = \frac{1}{\sqrt{T}}$. Fig. 2b shows the sample ACF of $G(t,f)$ using 2000 samples on a fixed subcarrier. As we can see from the figure, all the taps with positive time lags of the sample ACF are within the interval of $\pm 2\sigma_{\hat{\rho_G}(\tau,f)}$. Consequently, it can be assumed that $\varepsilon(t,f)$ is an additive white Gaussian noise, i.e., $\varepsilon(t,f) \sim \mathcal{N}(0,\sigma^2(f))$.

(3) Independence: At last, to verify that the power responses on different subcarriers are independent of each other, we compute the sample correlation coefficient among different subcarriers and depict the results in Fig. 2c. Since the sample correlation coefficient is close to zero for any two different subcarriers and $G(t,f)$ is Gaussian, it can be assumed that $\varepsilon(t,f_1)$ and $\varepsilon(t,f_2)$ are statistically independent, for $\forall f_1 \neq f_2$.

The above analysis on CSI measurement noise due to hardware imperfections is critical to deriving the theoretical false alarm rate, which is statistically irrelevant with environments, locations, orientations, and subjects, as will be presented in §4.2. Note that although previous works [23, 33] also explicitly or implicitly assume that the measurement noise is Gaussian, we are the first to formally and experimentally verify the soundness.

3.3 Modeling the Impact of Motion on CSI

Rationale for using statistical EM theory: Radio propagation in a building interior is in general very difficult to analyze because the EM waves can be absorbed and scattered by walls, doors, windows, moving objects, etc. However, buildings and rooms can be viewed as reverberation cavities in which they exhibit internal multipath propagations. Hence, we refer to a statistical modeling instead of a deterministic one and apply the statistical theory of EM fields developed for reverberation cavities [9] to analyze the statistical properties of the term $\mu(t,f)$.

Instead of assuming a limited number of reflection multipaths like existing works, we consider typical indoor space as a more realistic rich-scattering environment, where there could be hundreds or thousands of multipaths [8]. Fig. 3 illustrates a typical scenario, where a pair of Tx and Rx are deployed in the environment, both equipped with omnidirectional antennas. Various objects in the environment, e.g., walls, doors, humans, desks and other

furniture, can act as scatterers, which are diffusive and can reflect the impinging EM waves towards all directions. As a result, signals emitted by the Tx may be reflected, refracted, diffracted and then superimposed at the Rx. Our model is built upon an in-depth understanding of the statistical behaviors of EM wave propagation under such rich-scattering environments, rendering it truly multipath-resilient. The key result of the proposed statistical model for motion detection is as follows:

Remark 3. *The sample ACF of the power response $G(t, f)$ of a CSI measurement $H(t, f)$ approximates 0 for a static environment without motion and inversely remains above zero in presence of motion, within a sufficiently short time lag. The result holds as long as the time delay is short enough, regardless of the specific environment, motion location and orientation, and subject.*

In the following, we present the detailed derivation, from the perspective of statistical EM wave theory, of the proposed modeling of motion in CSI.

Decomposition of the received electric field: Denote the received electric field as $\vec{E}_{Rx}(t, f)$. Then, $\mu(t, f)$ actually measures the power of the received electric field, i.e., $\mu(t, f) = \|\vec{E}_{Rx}(t, f)\|^2$, where $\|\cdot\|^2$ denotes the Euclidean norm. $\vec{E}_{Rx}(t, f)$ can be decomposed into two parts as

$$\vec{E}_{Rx}(t, f) = \sum_{i \in \Omega_s(t)} \vec{E}_i(t, f) + \sum_{j \in \Omega_d(t)} \vec{E}_j(t, f) \tag{3}$$

where $\Omega_s(t)$ and $\Omega_d(t)$ denote the set of static scatterers and dynamic scatterers, respectively, and $\vec{E}_i(t, f)$ denotes the part of the received electric field scattered by the i-th scatterer. When the environment is static, $\Omega_d(t)$ is empty. The intuition behind the decomposition is that each scatterer can be treated as a "virtual antenna" diffusing the received EM waves in all directions as shown in Fig. 3, and then, these EM waves add up together at the receiving antenna after bouncing off human bodies, walls, ceilings, furniture, windows, etc.

Within a sufficiently short period, it is reasonable to assume that both the sets $\Omega_s(t)$, $\Omega_d(t)$ and the electric fields $\vec{E}_i(t, f)$, $i \in \Omega_s(t)$ change slowly in time. Then, we have the following approximation:

$$\vec{E}_{Rx}(t, f) \approx \vec{E}_s(f) + \sum_{j \in \Omega_d} \vec{E}_j(t, f), \tag{4}$$

where $\vec{E}_s(f) \approx \sum_{i \in \Omega_s(t)} \vec{E}_i(t, f)$.

As is known from the channel reciprocity, EM waves traveling in both directions will undergo the same physical perturbations (i.e. reflection, refraction, diffraction, etc.). Therefore, if the receiver were transmitting EM waves, all the scatterers would receive the same electric fields as they contribute to $\vec{E}_{Rx}(t, f)$. Therefore, in order to understand the properties of $\vec{E}_{Rx}(t, f)$, we only need to analyze its individual components $\vec{E}_i(t, f)$, which is equal to the received electric field by the i-th scatterer as if the Rx were transmitting. $\vec{E}_i(t, f)$ can be expanded in an orthogonal basis as $\vec{E}_i(t, f) = E_{i,x}(t, f)\hat{x} + E_{i,y}(t, f)\hat{y} + E_{i,z}(t, f)\hat{z}$, where $E_{i,u}(t, f)$ denotes the linear component of $\vec{E}_i(t, f)$ along the direction $\hat{u}$, $u \in \{x, y, z\}$, and $\hat{z}$ points to the moving direction of the scatterer.

ACF of the received electric field: Define the temporal ACF of a statistically stationary electric field $\vec{E}(t, f)$ along the direction $\hat{u}$ as

$$\rho_{E_u}(\tau, f) = \frac{\left\langle E_u(0, f) - \langle E_u(0, f)\rangle, E_u(\tau, f) - \langle E_u(\tau, f)\rangle \right\rangle}{\sqrt{\left\langle |E_u(0, f) - \langle E_u(0, f)\rangle|^2 \right\rangle \left\langle |E_u(\tau, f) - \langle E_u(\tau, f)\rangle|^2 \right\rangle}}, \tag{5}$$

where τ is the time lag, $\langle\ \rangle$ stands for the ensemble average over all realizations, $\langle X, Y\rangle$ denotes the ensemble average of XY^*, i.e., $\langle X, Y\rangle \triangleq \langle XY^*\rangle$, and $|E_u(t, f)|^2$ denotes the square of the absolute value of the electric field.

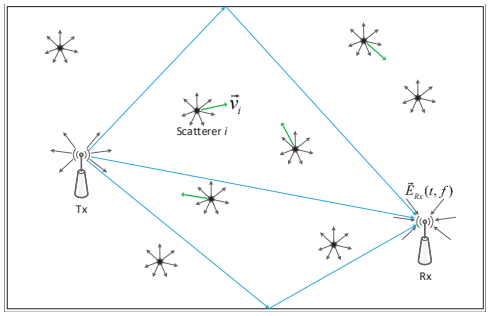

Fig. 3. Radio signal propagation in scattering environments.

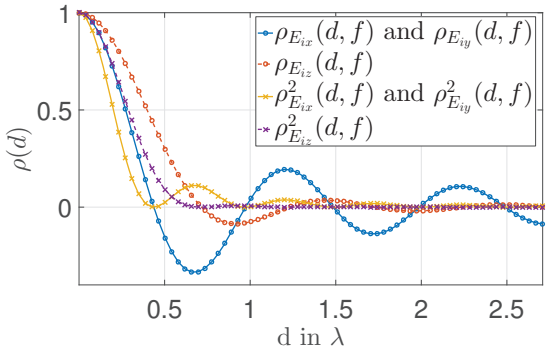

Fig. 4. Theoretical spatial ACF for different orthogonal components of EM waves.

Then, under certain common assumptions on the homogeneity of scattering for reverberation cavities [30][9], the ACF for each linear component of $\vec{E}_i(t,f)$ can be derived in closed forms as (we omit the detailed derivation here due to space limit)

$$\begin{aligned}\rho_{E_{i,x}}(\tau,f) &= \rho_{E_{i,y}}(\tau,f)\\ &= \frac{3}{2}\left[\frac{\sin(kv_i\tau)}{kv_i\tau}-\frac{1}{(kv_i\tau)^2}\left(\frac{\sin(kv_i\tau)}{kv_i\tau}-\cos(kv_i\tau)\right)\right], \qquad (6)\\ \rho_{E_{i,z}}(\tau,f) &= \frac{3}{(kv_i\tau)^2}\left[\frac{\sin(kv_i\tau)}{kv_i\tau}-\cos(kv_i\tau)\right], \qquad (7)\end{aligned}$$

where k is the wave number of the transmitted signal and τ denotes the time lag. By the change of variable $d \triangleq v_i\tau$, we can obtain the spatial ACF for each component which is independent of the speed of the scatterer. The numerical curves of the spatial ACF of $E_{i,u}$, for $u \in \{x,y,z\}$, are shown in Fig. 4. We can observe that the magnitudes of all the ACFs decay with oscillations as the scatterer moves away from its original location. The intuition behind is that it is assumed that the EM waves impinging each scatterer are uniformly distributed in the space and have equal energy. Integrating over all of the waves leads to the oscillating decay behavior of the distribution of the energy in the spatial domain around the scatterer. More detailed explanations and theoretical principles can be found in [7], [9] and [30].

Denote $E_i^2(f)$ as the radiation power of the i-th scatterer, $E_{s,u}^2(f)$ as the radiation power contributed by all the static scatterers along the direction $\hat{u}$, $E_d^2(f)$ as the variance of $\mu(t,f)$, and assume that $\vec{E}_{i_1}(t,f)$ and $\vec{E}_{i_2}(t,f)$ are statistically uncorrelated for $\forall i_1 \neq i_2$. Then, the ACF of the term $\mu(t,f)$ can be approximated as [30]

$$\begin{aligned}\rho_\mu(\tau,f) \approx \frac{1}{E_d^2(f)} \sum_{u\in\{x,y,z\}} \Bigg(\sum_{i\in\Omega_d} \frac{2E_{s,u}^2(f)E_i^2(f)}{3} \rho_{E_{i,u}}(\tau,f) \\ + \sum_{\substack{i_1,i_2\in\Omega_d \\ i_1\geq i_2}} \frac{E_{i_1}^2(f)E_{i_2}^2(f)}{9} \rho_{E_{i_1,u}}(\tau,f)\rho_{E_{i_2,u}}(\tau,f) \Bigg).\end{aligned} \tag{8}$$

The impact of the motion of each individual dynamic scatterer on the propagation of EM waves has been quantified in (8) based on the ACF of the power of the received electric field, and the influence of each dynamic scatterer on $\rho_\mu(\tau,f)$ is determined by the power of the electric field contributed by that scatterer. An important observation is that when $\tau \to 0$, we have $\rho_\mu(\tau,f) \to 1$. This is because $\rho_{E_{i,u}}(\tau,f)$, for $\forall i \in \Omega_d$ and $\forall u \in \{x, y, z\}$, is continuous at point $\tau = 0$ as shown in (6) and (7). In addition, the variance $E_d^2(f)$ measures the power reflected by all the dynamic scatterers and it can be expressed as a function of the power reflected by each individual dynamic scatterer:

$$E_d^2(f) = \sum_{u\in\{x,y,z\}} \Bigg(\sum_{i\in\Omega_d} \frac{2E_{s,u}^2(f)E_i^2(f)}{3} + \sum_{\substack{i_1,i_2\in\Omega_d \\ i_1\geq i_2}} \frac{E_{i_1}^2(f)E_{i_2}^2(f)}{9} \Bigg). \tag{9}$$

As $\mu(t,f)$ is due to the propagations of EM waves and $\varepsilon(t,f)$ is due to the imperfect measurements of CSI, it can be assumed that $\mu(t,f)$ and $\varepsilon(t,f)$ are uncorrelated with each other, i.e., $\mathrm{cov}(\mu(t_1,f),\varepsilon(t_2,f)) = 0$, for $\forall t_1, t_2$, Therefore, the auto-covariance function of $G(t,f)$ can be expressed as

$$\begin{aligned}\gamma_G(\tau,f) &\triangleq \mathrm{cov}\Big(\mu(t,f)+\varepsilon(t,f), \mu(t-\tau,f)+\varepsilon(t-\tau,f)\Big) \\ &= E_d^2(f)\rho_\mu(\tau,f) + \sigma^2(f)\delta(\tau),\end{aligned} \tag{10}$$

where $\delta(\cdot)$ is Dirac delta function. The corresponding ACF of $G(t,f)$ can thus be expressed as

$$\rho_G(\tau,f) = \frac{E_d^2(f)}{E_d^2(f)+\sigma^2(f)}\rho_\mu(\tau,f) + \frac{\sigma^2(f)}{E_d^2+\sigma^2(f)}\delta(\tau). \tag{11}$$

From (11), we make the following important observations:

Remark 4. *In presence of motion, if $\tau \to 0$, we already know $\rho_\mu(\tau,f) \to 1$ and thus we have $\rho_G(\tau,f) \to \frac{E_d^2(f)}{E_d^2(f)+\sigma^2(f)} > 0$; when there is no motion and $\tau \to 0$, we have $\rho_G(\tau,f) = 0$ since $E_d^2(f) = 0$.*

The above result is a formal description of Remark 3. Therefore, $\lim_{\tau\to 0}\rho_G(\tau,f)$ is a good statistical indicator of the presence of motion, which is only determined by $E_d^2(f)$ incurred by motion and the power of the measurement noise $\sigma^2(f)$ and is independent of environments, locations, orientations, and subjects. We will leverage this important observation to design an accurate and robust motion detector, as detailed in the next section (§4).

3.4 Model Verification with Real-world Data

In the following, before we present how to detect motion based on the proposed statistical model of CSI, we first analyze and verify the model via real-world data measured by commodity WiFi devices.

For a typical WiFi channel with a carrier frequency of 5.8 GHz, the maximum difference in the wavenumber $k = 2\pi/\lambda$ of different subcarriers is within 1% and thus can be neglected. Hence, under the proposed statistical model, we are expecting that 1) the ACF of each scatterer $\rho_{E_i,u}(\tau, f)$ is frequency-independent, i.e., $\rho_{E_i,u}(\tau, f_1) \approx \rho_{E_i,u}(\tau, f_2)$, for $\forall f_1, f_2 \in \mathcal{F}$, $u \in \{x, y, z\}$ and $\forall i \in \Omega_d$; and that 2) $E_{s,u}(f)$ and $E_i(f)$ can be approximated as flat-fading within a sufficient small bandwidth.

To verify, we set up a WiFi link by putting the Tx and Rx about 5 meters away. Both Tx and Rx are commodity WiFi devices equipped with 3 omnidirectional antennas and operate on channel 161 with a center frequency of $f_c = 5.805$ GHz, and bandwidth of 40 MHz. The channel sampling rate F_s is set to 1000 Hz. Note such a high sampling rate is only used for model verification. WiDetect works gracefully with a sampling rate as low as 30 Hz (See Section 5). During data collection, a person first keeps static for about 1.5 seconds, and then walks at a nearly constant speed, and finally stops and keeps static for another 1 second. The total duration is about 10 seconds.

The power responses $G(t, f)$ of all the subcarriers for an antenna pair are plotted in Fig. 5a, where CSI is measured on 114 subcarriers indexed as $\{1, 2, \cdots, 114\}$. Each column of the image shows the power responses measured on different subcarriers at some time instant. As we can see from Fig. 5a, the power responses become visually blurred when human walking nearby. The variations of the power responses induced by motion will be modeled and analyzed in Section 3.3. Fig. 5b-5d show the power responses of three typical subcarriers for $t \in [5, 5.25]$ s with subcarrier index $f_1 = 1$, $f_2 = 5$, and $f_3 = 9$ separately. Since the spacing of the adjacent subcarriers is 312.5 KHz, the chosen subcarriers are separated by 1.25 MHz. As we can see from the figures, the power response of each subcarrier exhibits a long-term trend and short-term changes which is superimposed on the trend. To satisfy the conditions of stationarity, $G(t, f)$ is detrended by the subtraction of its linear trends computed by smoothing $G(t, f)$, as shown in Fig. 5e-5g, respectively. Then the ACFs of the detrended power responses are calculated and depicted in Fig. 5h-5j. As seen, although $G(t, f_i)$, $i = \{1, 2, 3\}$, are quite different in terms of shapes, they exhibit similar ACFs, which is already predicted by our proposed statistical model. From (8), we know that $\rho_\mu(\tau, f)$ is a continuous function which consists of damped sinusoid functions, and the form of the ACF of $G(t, f)$ is given in (11), which agrees well with the observations in Fig. 5h-5j. Note that the autocorrelation corresponding to the time lag close to 0 experiences a sudden drop for each case as explained in (11). Recall that when there is no motion in the environment, the ACF is close to 0 for all the non-zero time lags, as shown in Fig. 2b.

In a nutshell, these experimental observations agree well with the theoretical results, which validates the assumptions in the above analysis and verifies the correctness and effectiveness of the proposed model.

4 WIDETECT DESIGN

In this section, we present the detailed design of WiDetect, a motion detection technology that turns a WiFi radio into a motion sensor that is capable of sensing motion accurately and robustly at a whole-home scale. Specifically, we propose a novel motion statistic based on the proposed statistical model as a measure of the likelihood of motion presence and accordingly design a simple yet effective motion detector.

4.1 Motion Statistics

Note that when time lag τ approaches 0 and the environment is dynamic, according to (11), for each subcarrier $f \in \mathcal{F}$, we have

$$\begin{aligned} \lim_{\tau \to 0} \rho_G(\tau, f) &= \lim_{\tau \to 0} \frac{E_d^2(f)}{E_d^2(f) + \sigma^2(f)} \rho_\mu(\tau, f) \\ &= \frac{E_d^2(f)}{E_d^2(f) + \sigma^2(f)}. \end{aligned} \tag{12}$$

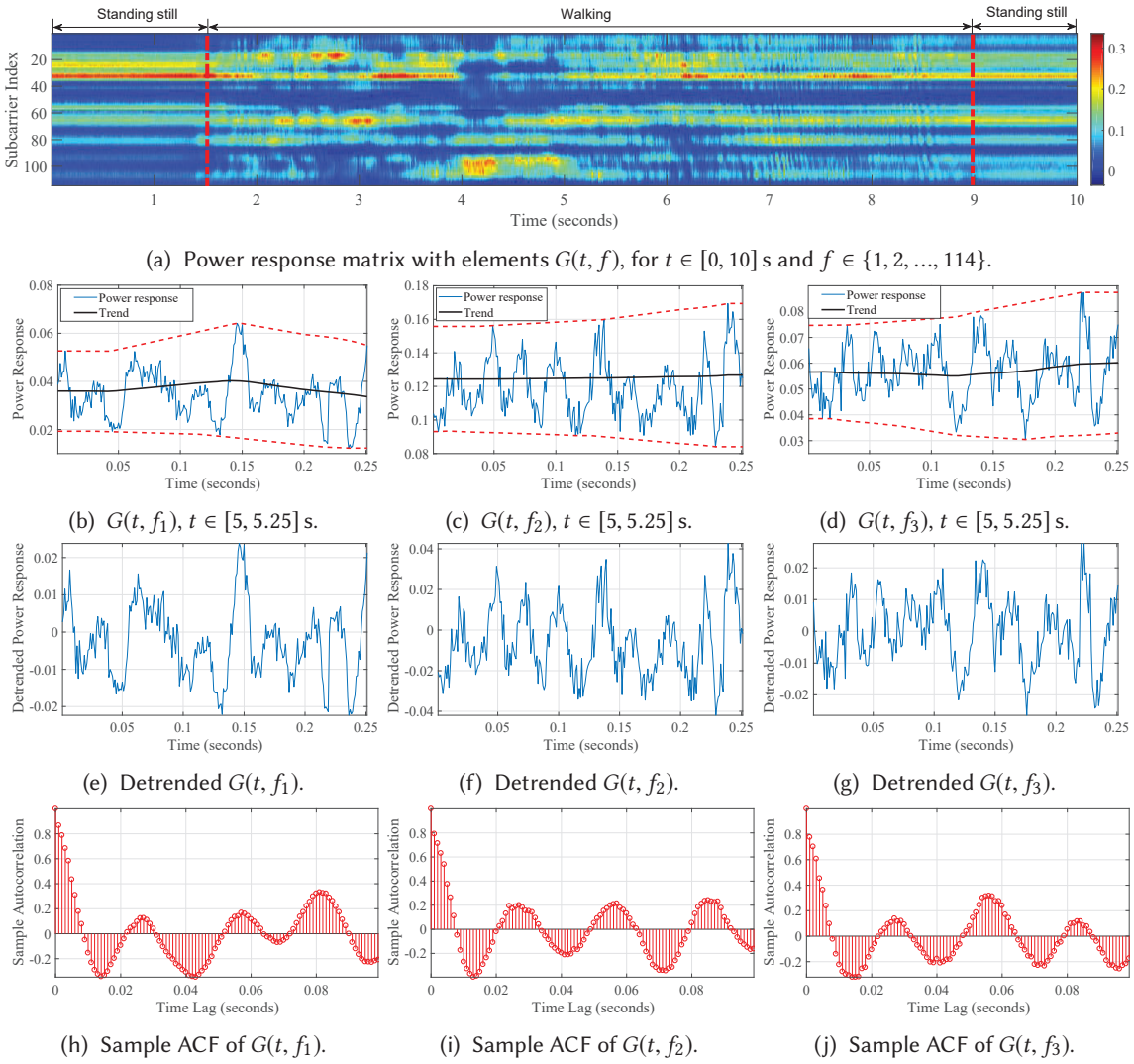

(a) Power response matrix with elements $G(t, f)$, for $t \in [0, 10]$ s and $f \in \{1, 2, ..., 114\}$.

(b) $G(t, f_1)$, $t \in [5, 5.25]$ s. (c) $G(t, f_2)$, $t \in [5, 5.25]$ s. (d) $G(t, f_3)$, $t \in [5, 5.25]$ s.

(e) Detrended $G(t, f_1)$. (f) Detrended $G(t, f_2)$. (g) Detrended $G(t, f_3)$.

(h) Sample ACF of $G(t, f_1)$. (i) Sample ACF of $G(t, f_2)$. (j) Sample ACF of $G(t, f_3)$.

Fig. 5. Power responses and sample ACFs on different subcarriers. (a) shows the power response matrix for 10 seconds with a sampling rate of 1000 Hz. (b-d) show the raw power responses and their trends for three typical subcarriers. (e-g) show the detrended power responses for the selected subcarriers, and (h-j) show the corresponding ACF estimates.

If the environment is static, we have $\lim_{\tau \to 0} \rho_G(\tau, f) = 0$, since $\rho_\mu(\tau, f) = 0$ for $\forall \tau \neq 0$. Therefore, the quantity $\lim_{\tau \to 0} \rho_G(\tau, f)$ is a good indicator of the presence of the motion in the environment, which is only determined by the power of motion $E_d^2(f)$ and the power of measurement noise $\sigma^2(f)$ and is independent of the moving speed of the dynamic scatterers. However, $\lim_{\tau \to 0} \rho_G(\tau, f)$ cannot be measured directly due to the limitation of the channel sampling rate F_s. Instead, we use the quantity $\rho_G\left(\tau = \frac{1}{F_s}, f\right)$ as an approximation of $\lim_{\tau \to 0} \rho_G(\tau, f)$ as long as F_s is large enough. Then we define a motion statistic as follows:

Definition 1. *The motion statistic $\phi(f)$ on subcarrier f is defined as*

$$\phi(f) \triangleq \rho_G\Big(\tau = \frac{1}{F_s}, f\Big), \tag{13}$$

which can be estimated from the power response measurements $G(t, f)$ as

$$\hat{\phi}(f) = \frac{\hat{\gamma}_G\Big(\tau = \frac{1}{F_s}, f\Big)}{\hat{\gamma}_G(\tau = 0, f)}, \tag{14}$$

where $\hat{\gamma}_G(\tau, f)$ is defined in (2).

When there is no motion in the environment, we have $\phi(f) = 0$; when there is motion, we have $\phi(f) \in (0, \frac{E_d^2(f)}{E_d^2(f)+\sigma^2(f)})$ and $\phi(f)$ approaches to $\frac{E_d^2(f)}{E_d^2(f)+\sigma^2(f)}$ only when both the sampling rate F_s and the number of samples are sufficiently large.

Suppose that the channel is sampled with equal intervals and there are T measurements in total. Without loss of generality, we can arrange the measured power responses as $G(t, f)$, for $t = 0, \frac{1}{F_s}, \ldots, \frac{T-1}{F_s}$ and $f = 1, \ldots, F$. When there is no motion in the environment, it is already shown in Sec. 3.2 that the power response on each subcarrier f follows a Gaussian distribution with a constant mean, i.e., $G(t, f) \sim \mathcal{N}(\mu(f), \sigma^2(f))$, where we define the constant as $\mu(f) \triangleq \mu(t, f)$, for $\forall t$. Furthermore, when T is large enough, the sample ACF of $G(t, f)$ can be approximated as a Gaussian random variable with mean $-\frac{1}{T}$ and $\frac{1}{T}$ as the variance, i.e., $\hat{\rho}_G(\tau, f) \sim \mathcal{N}(-\frac{1}{T}, \frac{1}{T})$ for $\forall \tau \neq 0$. Specifically, for the case $\tau = \frac{1}{F_s}$, the distribution of the estimation of the proposed motion statistic $\phi(f)$ is thus obtained as $\hat{\phi}(f) \sim \mathcal{N}(-\frac{1}{T}, \frac{1}{T})$. Since the noise term $\varepsilon(t, f)$ is independent for different subcarriers, the estimated motion statistic $\hat{\phi}(f), \forall f \in \mathcal{F}$, is thus independent and identically distributed random variables. Note that the distribution of $\hat{\phi}(f)$ is only a function of the sample size T and is not affected by the variance of measurement noise $\sigma^2(f)$. Therefore, the variation of $\sigma^2(f)$ due to the imperfection of the circuits will not affect the statistical behaviors of $\hat{\phi}(f)$ when no motion is present in the environment.

4.2 Detection Rule

Motion detection can be formulated as a hypothesis testing problem:

$$\begin{aligned} \mathcal{H}_0: &\quad \hat{\phi}(f) \sim \mathcal{N}(-\frac{1}{T}, \frac{1}{T}),\ \forall f \in \mathcal{F}, \\ \mathcal{H}_1: &\quad \hat{\phi}(f) \to \frac{E_d^2(f)}{E_d^2(f) + \sigma^2(f)} > 0,\ \forall f \in \mathcal{F} \end{aligned} \tag{15}$$

where $\mathcal{H}_0$ denotes the null hypothesis when there is no motion in the monitored environment, and $\mathcal{H}_1$ denotes the alternative hypothesis when motion happens.

We define the average of motion statistic as $\hat{\psi} = \frac{1}{F}\sum_{f=1}^{F}\hat{\phi}(f)$. Since $\hat{\phi}(f)$'s are independent and identically distributed for different subcarriers, the distribution of the sample average of $\hat{\phi}(f)$ over F subcarriers can be approximated as $\hat{\psi} \sim \mathcal{N}(-\frac{1}{T}, \frac{1}{FT})$, that is, the variance of $\hat{\psi}$ is inversely proportional to the number of samples T and the number of subcarriers F. At the same time, since the motion statistic $\hat{\phi}(f)$ is a positive number when there is motion in the environment, a simple detection rule is proposed for the detection of the presence of motion: given a preset threshold η, if $\hat{\psi}$ is greater than or equal to η, than WiDetect reports a detection of motion; otherwise, no motion is detected.

On this basis, we can theoretically build the false alarm rate under the hypothesis $\mathcal{H}_0$ and a given preset threshold η:

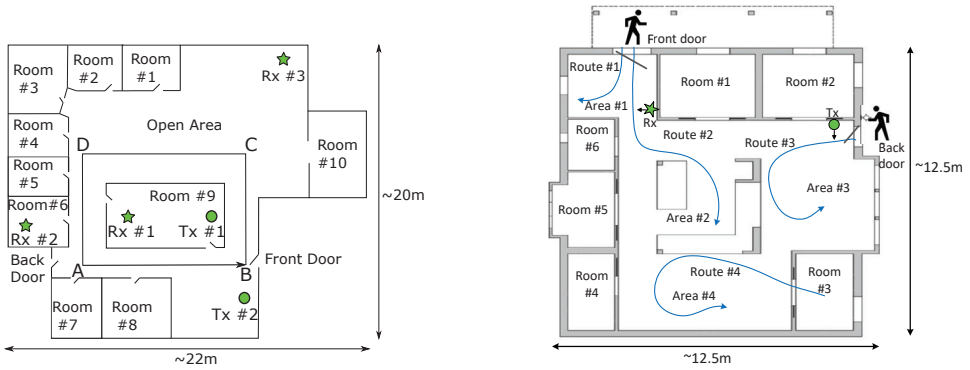

(a) A typical office. (b) A typical single house.

Fig. 6. Floorplans of two different environments.

Remark 5. *The probability of false alarm can be approximated as*

$$P(\hat{\psi} > \eta) = Q\Big(\sqrt{FT}\big(\eta + \frac{1}{T}\big)\Big), \tag{16}$$

where $Q(\cdot)$ denotes the Q-function, which is the tail probability of the standard normal distribution, i.e., $Q(x) = \frac{1}{2\pi}\int_x^\infty \exp(-\frac{u^2}{2})\,\mathrm{d}u$.

For the detection probability of WiDetect, it is hard to characterize it theoretically since $\hat{\phi}(f)$ is determined by $E_d^2(f)$, which is dependent on the location of motion, and $\sigma^2(f)$, which is dependent on the working condition of the WiFi chipsets. However, when there is no motion, the statistical behavior of $\hat{\psi}$ is only a function of F and T, which is independent of the variance of the measurement noise $\sigma^2(f)$.

5 EXPERIMENTAL EVALUATION

To evaluate the performance of WiDetect, we implement a real-time system on Intel Galileo Gen2 board using a pair of commercial WiFi devices, one as Tx and the other as Rx. Each WiFi device is equipped with 3 omnidirectional antennas, and each stream over a pair of antennas has a total of 114 subcarriers. By default, the system works on channel 161 with a carrier frequency of 5.805 GHz and bandwidth of 40MHz. We deploy the system in three different scenarios for evaluation:

- We first test WiDetect in a common office (Fig. 6a) to validate the performance and study different factors that may impact the performance.
- We further evaluate the accuracy and coverage in a single house with 6 rooms (Fig. 6b) for a period of one week. PIR sensors are also installed inside the house for comparison.
- Furthermore, we deploy WiDetect in a one-bedroom apartment for one month to monitor long-term motion and demonstrate its potential to analytical applications based on the motion detection results.

The prototype system is built on two compact embedded devices so that it can be easily deployed for long-term evaluation.

5.1 Detection Accuracy

We first verify the theoretical analysis described in Section 4, and verify the performance of the proposed detection rule of WiDetect using the same WiFi channel as stated in Sec. 3.4. For validation, the sampling rate F_s is set to

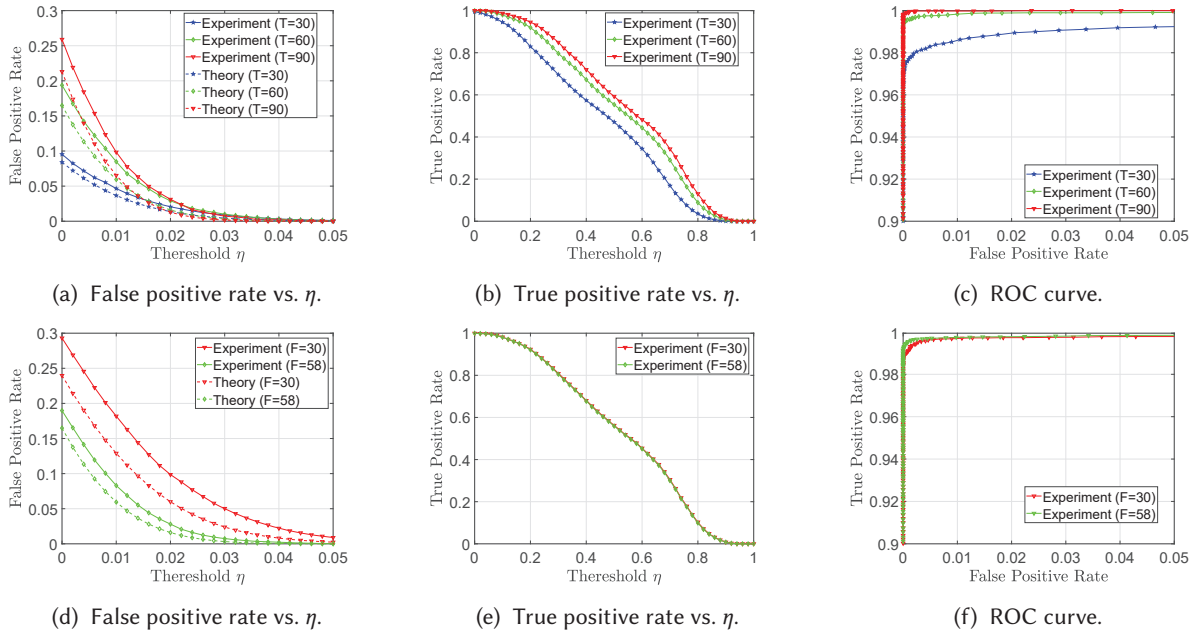

(a) False positive rate vs. η. (b) True positive rate vs. η. (c) ROC curve.

(d) False positive rate vs. η. (e) True positive rate vs. η. (f) ROC curve.

Fig. 7. Performance of the proposed WiDetect for different window size T and number of subcarriers F.

180 Hz. The Tx and Rx devices are placed at location Tx #2 and Rx #2, respectively, as shown in Fig. 6a. One subject first walks inside Room #9 for 30 minutes, and then walks outside Room #9 but within the square $A-B-C-D$ indicated in Fig. 6a for another 30 minutes. At last, we collect a set of one-hour CSI data when the environment is static and no one is inside the office.

Impact of sample size and the number of subcarriers: We calculate the false positive rate using the experimental CSI data and compare with the theoretical false alarm probability according to (16). The comparison is shown in Fig. 7a for different sample sizes T and in Fig. 7d for different number of subcarriers F, respectively, with varying η. The theoretical curves match well with the experimental ones when η is greater, and the gap at smaller η is due to the correlation among different subcarriers, which we assume not existing in the theoretical analysis. As for the detection probability, Fig. 7b shows that increasing T improves the detection probability for a fixed η and Fig. 7e indicates that increasing F has no effect on the detection probability. The ROC curves in Fig. 7c and Fig. 7f show that the performance of WiDetect improves as T and F increase.

Impact of sampling rate: From the analysis in Section 4.1, a higher sampling rate F_s is preferred, and the higher the sampling rate, the larger the motion statistic can be obtained when motion exists. The normalized histograms of $\hat{\psi}$ in the above-mentioned three scenarios with varying channel sampling rate F_s are shown in Fig. 8, and the corresponding RoC curves are also shown in Fig. 9. As we can observe from Fig. 8, the average of the motion statistic $\hat{\psi}$ increases as the sampling rate increases when there exists motion, which facilitates the detection of the presence of the motion and also agrees with the results shown in Fig. 9. However, in practice, a higher sampling rate would incur a larger interference to the existing WiFi network. As a result of the trade-off, we set a channel sampling rate as $F_s = 30$Hz in the following experiments. Furthermore, when motion occurs more closely to one of the devices, $\hat{\psi}$ becomes larger as well. This is because the energy E_d^2 of the EM waves reflected off the moving human body is larger due to a smaller path loss when the human body is close to the transmission pair.

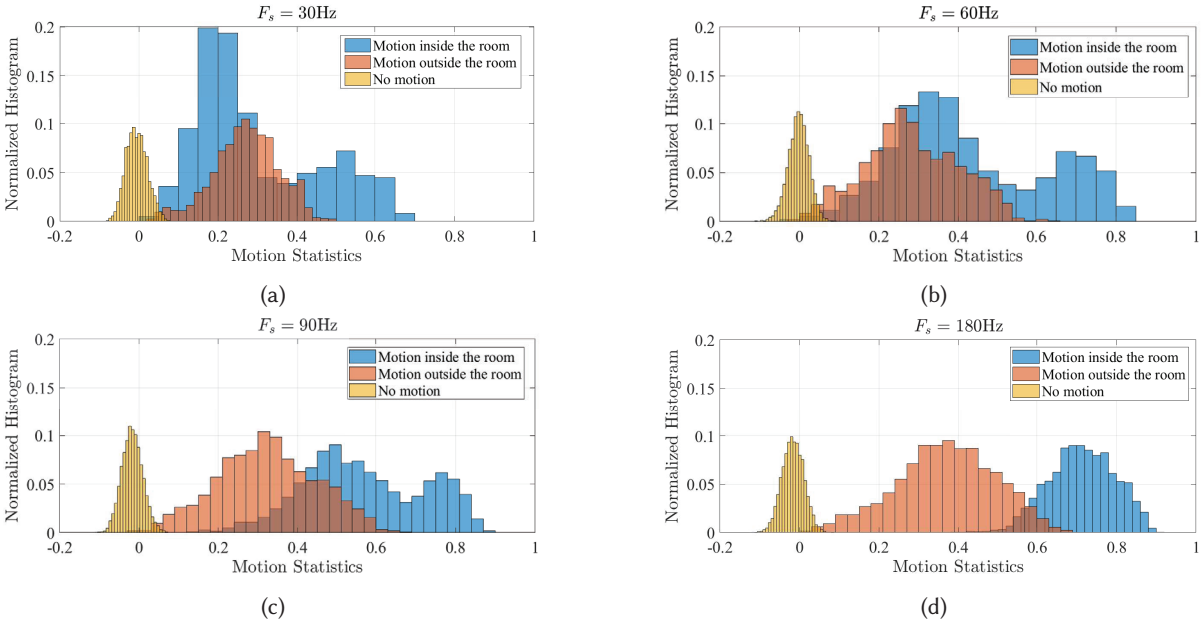

Fig. 8. The normalized histogram of $\hat{\psi}$ under three conditions: motion inside of the room, motion outside of the room and no motion indoors with $T = 60$ and $F = 58$. The sampling rate of (a) - (d) is set to 30 Hz, 60 Hz, 90 Hz, and 180 Hz, respectively.

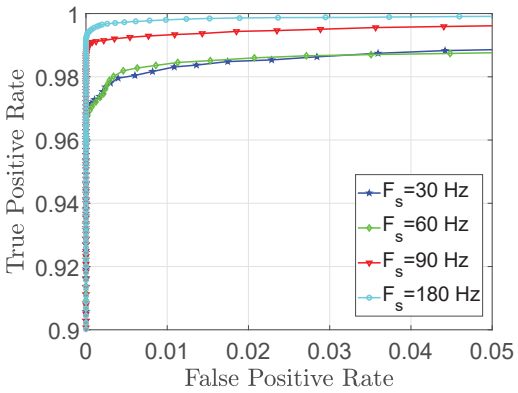

Fig. 9. The ROC curves of WiDetect for different sampling rate.

Comparative study: We have also compared the performance of WiDetect with two state-of-art systems, DeMan [23] and SIED [12], using the same data set described in the above. DeMan exploits the observation that the value of the normalized maximum eigenvalue, i.e., λ_{max}, of the CSI correlation matrix drops below 1 when the CSIs fluctuate temporally; SIED captures the variance of variances of amplitudes of each subcarrier, which directly measures the variations of the CSIs over time. All compared systems output one decision every second, using the same parameter settings ($T = 60$ and $F_s = 30$Hz) and the same number of subcarriers. Fig. 10 shows an

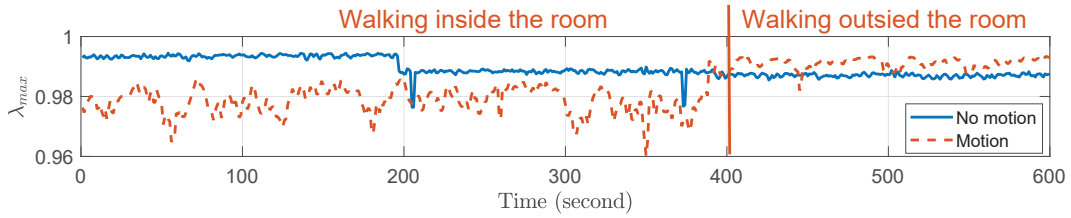

(a) Motion metric proposed in DeMan: the normalized maximum eigenvalue λ_{max}.

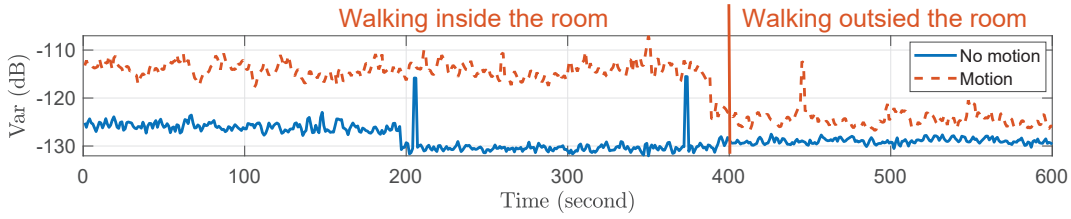

(b) Motion metric proposed in SIED: the variance of variances of amplitudes of each subcarrier.

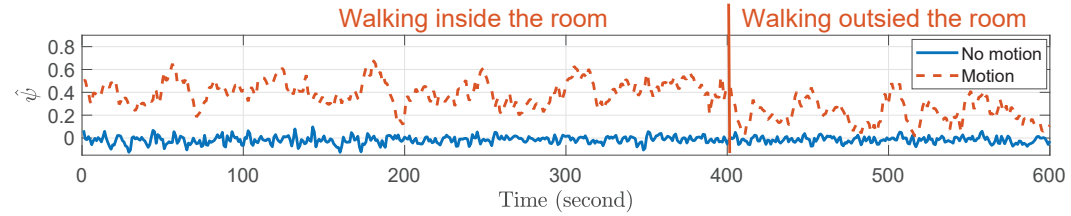

(c) Motion metric proposed in WiDetect: the motion statistic.

Fig. 10. An illustration for the comparison among (a) DeMan, (b) SIED, and (c) WiDetect. For *no motion* case: the environment is static for 600 seconds; for *motion* case: walking inside Room #9 for $t \in [0, 400]s$ and walking outside Room #9 for $t \in [401, 600]s$.

illustration of the behavior of the motion metrics proposed in WiDetect, SIED and DeMan under the scenarios with and without motions respectively. When no motion exists, the motion metrics proposed by the data-driven approaches, e.g., SIED and DeMan, are piecewise constant and the level changes from time to time due to the change of the variance of the noise of the measured CSI, making them less robust and difficult to choose proper parameters. In addition, a few large spikes are observed which are induced by RF interference. By contrast, the proposed motion statistic (13) in WiDetect is not affected by the measurement noise of CSI and is only determined by the sample size and the number of subcarriers as discussed in Section 4.1. This is because WiDetect implicitly exploits the property that the measurement noise is white in the time domain (see Section 3.2), and the variance of noise has only an influence on the motion statistic when motion exists (see (15)). The ROC curves of these three approaches are also calculated and compared in Fig. 11. As seen, WiDetect significantly outperforms the other two. Specifically, for a fixed false alarm 0.001, which implies that one false alarm is expected for every 1000 seconds in average, the corresponding detection rate of WiDetect is 0.995, while SIED and DeMan only achieve a detection rate of 0.893 and 0.691, respectively.

Impact of carrier frequency: WiDetect is applicable for all of the available WLAN channels. To demonstrate it, one dual-band Tx and two Rx's are placed at location Tx #1 and Rx #1, respectively, as shown in Fig. 6a. The Tx keeps transmitting with a sampling rate of 30Hz on both 2.4GHz and 5GHz channels simultaneously, and

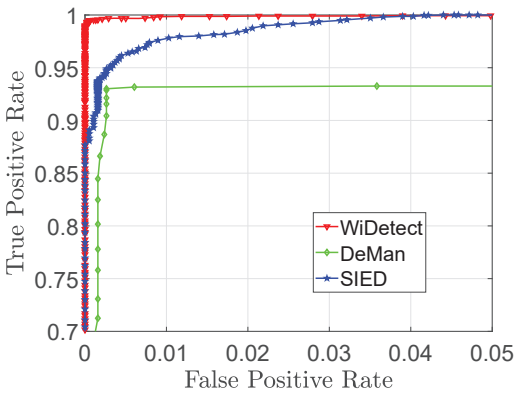

Fig. 11. The comparison of ROC curves among DeMan, SIED and WiDetect.

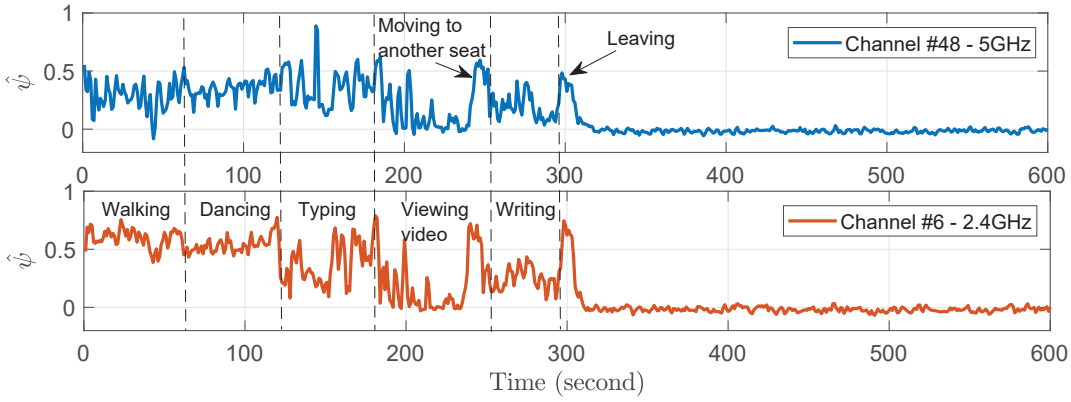

Fig. 12. Motion statistics side-by-side comparison: 2.4GHz vs. 5GHz WLAN channel. Activities include walking, dancing, typing keyboards, viewing video on a smartphone and writing on paper.

two co-located Rx's keep listening to the two channels separately. Five different activities, i.e., walking, dancing, typing keyboards, viewing a video on a smartphone and writing on paper, are performed, and the period of each activity is denoted in Fig. 12. It is shown that the motion statistic estimated on both channels exhibits consistent patterns (which is expected for the same motion source), and both of them are very sensitive to the motion induced by different activities. It can be observed that the motion statistic measured on 2.4GHz band is slightly larger than those measured on 5GHz band. This is because the wavelength of 2.4GHz-band signals is longer and thus the motion statistic experiences a less loss for the same moving objects, as shown in Fig. 4.

Impact of motion types: WiDetect is designed to push the limit of motion detection for general moving objects, not just human. To verify this, we have conducted various experiments to monitor the motion of different objects, such as an oscillating electric fan, a working iRobot Roomba 880, and a medium-sized cat. Fig. 13 shows that WiDetect detects all different types of motion. Specifically, 1) the motion statistic of an oscillating fan exhibits repetitive patterns and the frequency agrees with that of the rotating fan head, which is about 10 cycles per minute; 2) the motion statistic of a working Roomba exhibits irregular patterns since the Roomba moves randomly

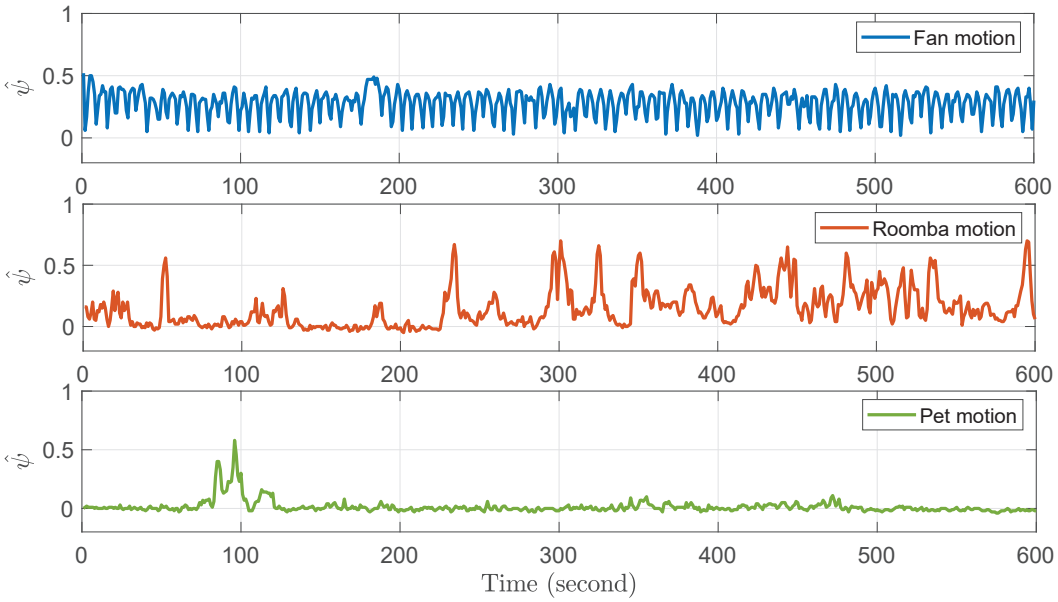

Fig. 13. Motion statistics for different motion types: an oscillating electric fan, iRobot Roomba, and a medium-sized cat.

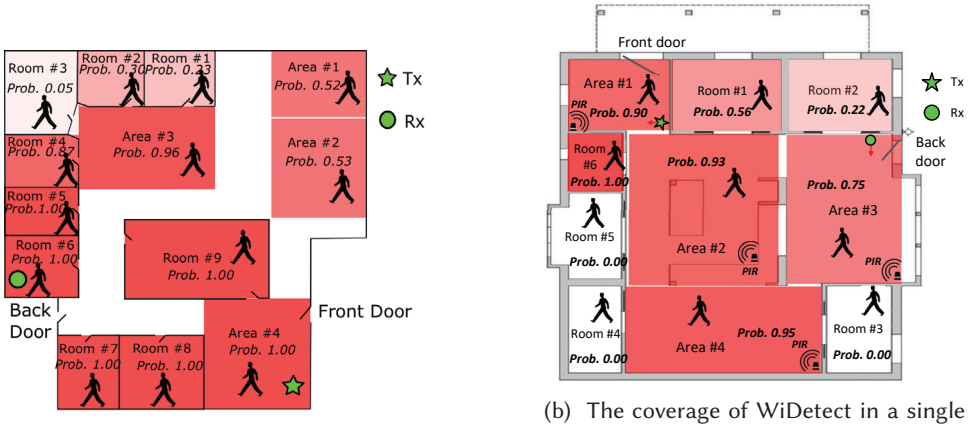

(a) The coverage of WiDetect in an office.

(b) The coverage of WiDetect in a single house.

Fig. 14. The coverage of WiDetect in two different environments.

in the room; 3) the motion statistic of a medium-sized cat is small most of the time since the cat is very quiet and has few activities usually. In practice, if it is not of interest to detect non-human motion, which is the common case for security applications like intruder detection, then different features, such as the periodicity, mean and variance, could be extracted from the estimated motion statistic to recognize the types of motion. However, motion type recognition is out of the scope of this paper and we leave it to future work.

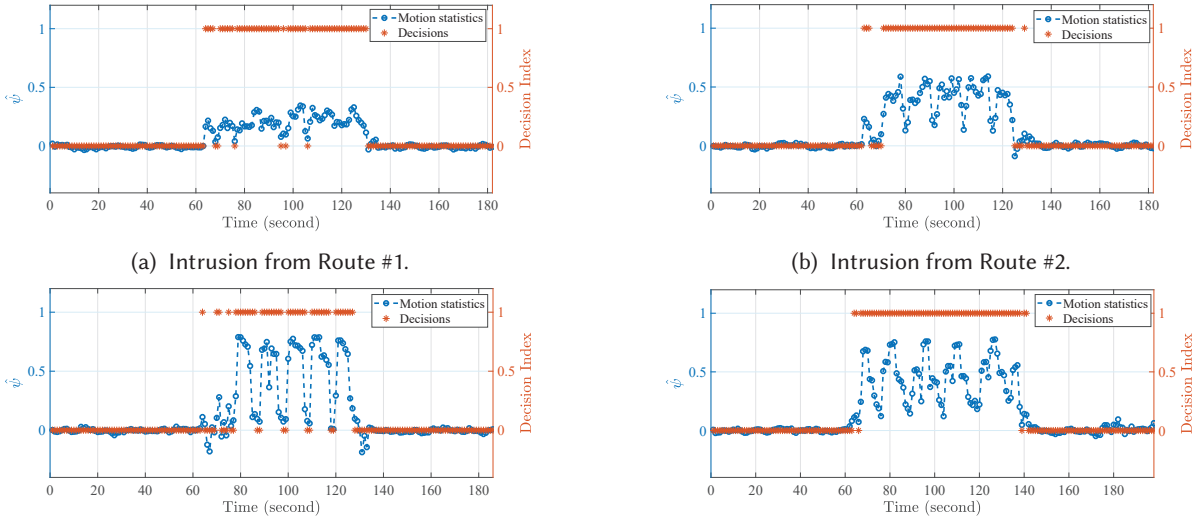

(a) Intrusion from Route #1.

(b) Intrusion from Route #2.

(c) Intrusion from Route #3.

(d) Intrusion from Route #4.

Fig. 15. Experimental results for intrusion tests with different preset routes.

In the following experiments, the parameters $\eta = 0.1$, $T = 60$ and $F_s = 30$Hz are applied in WiDetect and all the available subcarriers from the 3×3 antenna pairs are utilized for evaluation.

5.2 Coverage

Table 3. Empirical detection probability (EDP) for Different Routes in Fig. 6b

Route	#1	#2	#3	#4
EDP	0.90	0.98	0.83	1

To test the coverage of WiDetect, one subject walks in different regions of an office and a single house as shown in Fig. 6, respectively. The positions of the Tx and Rx are also indicated on the floorplan, and both of them are placed near the doors for more timely detection of intrusions. We define the empirical detection probability (EDP) of a region as the ratio between the duration when motion is detected and the total time when motion is present in that region. The corresponding results are summarized in Fig. 14a and Fig. 14b, which show that the motion occurring in most of the areas of the office and the house can be detected by the deployed single pair of WiFi devices except for a few rooms too far away from the transmission pair. In some regions, such as Room #1 and #2 in Fig. 14a, the detection rate is relatively lower. This is because in this experiment, the devices are placed vertically against the wall and the mounted antennas are facing towards the opposite directions to these two rooms. Note that due to the multipath effect of the propagations of EM waves, and the energy of the transmitted signal is not uniformly distributed in the environment. Therefore, the detection rate may be very high for some area that are far away from both the Tx and Rx, e.g., Area #4 in Fig. 14b. In practice, however, as long as there is at least one motion detected along the subject's moving trajectory, the presence of that moving subject can be detected.

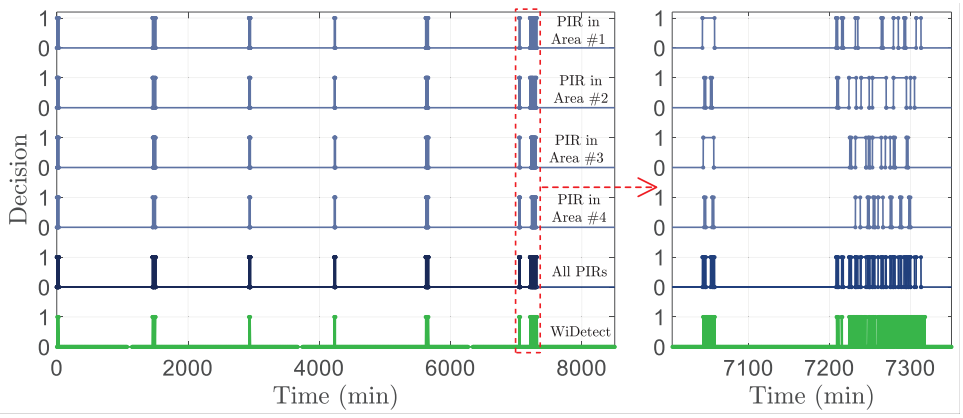

Fig. 16. Experimental results for long-term test compared with PIRs. Even the fused results (the 5th row) from 4 PIR sensors do not produce as good detection rate as WiDetect (the last row) due to the LOS limitation of PIR system.

To further demonstrate this, we ask a user to act as an intruder who "breaks" into the house following four different routes as indicated in Fig. 6b, and then leaves the house following the same route. The motion statistic and the corresponding decisions are calculated and shown in Fig. 15. We then evaluate the EDP for each individual route and illustrate the results in Table 3. The results show that the presence of the "intruder" can be detected most of the time for different routes.

5.3 Real-world Long-term Study

Comparison with commercial PIR system: To evaluate the false alarm rate, we run WiDetect in the same single house for one week and compare with the detection system that deploys 4 PIRs in different areas of the house. A participant is asked to enter the house every day and keeps a record of his activity as the groundtruth. The detection results for both WiDetect and the 4 PIRs are shown in Fig. 16, where an even decision index 0 indicates that no motion is detected and 1 indicates that motion is detected. It shows that 99.68% percent of the recorded motion has been successfully detected by WiDetect, while only 86.80% percent of the motion is detected by the four PIRs (Each PIR sensor can only detect motion in a certain direction and thus their detection results are integrated together as a whole system). No false alarms have been observed for both of the two systems during the whole week. The results show that WiDetect can achieve comparable detection performance as the PIRs while having much larger coverage. In addition, WiDetect can output one decision every single second, achieving a much higher time resolution in motion detection compared with the commercial PIRs.

Daily liveliness monitoring: Furthermore, WiDetect is also installed in an apartment with a couple living normally inside for one month. To show the patterns of the residents' daily activities, only the percentage of the motion detected within each hour is shown in Fig. 17. As we can see from the figure, denser motions are observed during weekends when the users stay at home for most of the time, while usually no motion is reported during typical working hours in weekdays. Looking at a specific working day, one can easily see when the residents go to work and come back home. Comparing the four weeks throughout the monitoring period, such repetitive patterns can be obviously observed due to the the residents' routine activities. These results demonstrate that the user's lifestyle can be clearly revealed from the motion detection results of WiDetect, which inspires many interesting research problems such as home security monitoring, physical analytics, and smart building monitoring for our future works.

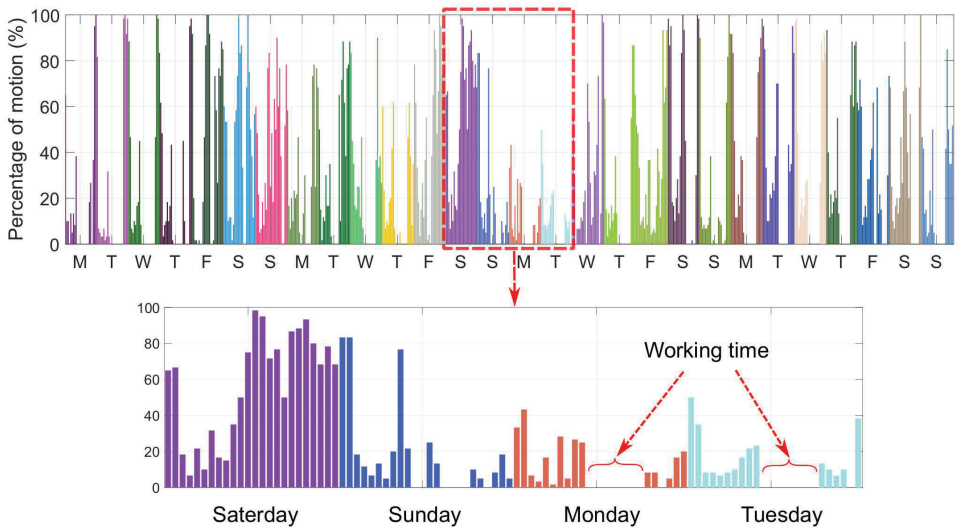

Fig. 17. Motion monitoring for one month. Each color indicates the monitoring results for an individual day from 00:00am to 23:59pm.

6 CONCLUSIONS

In this work, we present the model, design, and implementation of WiDetect, the first whole-home motion detection system that achieves almost zero false alarms using only a single WiFi link. A statistical model, from a refreshing perspective of statistical EM waves, that comprehensively leverages all existing multipath components for motion detection is proposed. Extensive experiments show its superiority over existing motion detection approaches. With extremely high sensitivity and fairly low false alarms, we believe that the proposed WiDetect can be a promising practical technology for ubiquitous device-free motion detection, allowing for a range of critical applications for a smart life.

ACKNOWLEDGMENTS

We would like to thank the anonymous reviewers for their valuable comments for improving the quality of the paper. We also thank the volunteers in our group who helped us in collecting the motion dataset.

REFERENCES

[1] Fadel Adib, Zach Kabelac, Dina Katabi, and Robert C. Miller. 2014. 3D Tracking via Body Radio Reflections. In *11th USENIX Symposium on Networked Systems Design and Implementation*. USENIX Association, 317–329.
[2] Eric Blossom. 2004. GNU radio: tools for exploring the radio frequency spectrum. *Linux journal* 2004, 122 (2004), 4.
[3] George EP Box, Gwilym M Jenkins, Gregory C Reinsel, and Greta M Ljung. 2015. *Time series analysis: forecasting and control*. John Wiley & Sons.
[4] Chen Chen, Yan Chen, Yi Han, Hung-Quoc Lai, Feng Zhang, and K. J. Ray Liu. 2017. Achieving centimeter-accuracy indoor localization on WiFi platforms: A multi-antenna approach. *IEEE Internet of Things Journal* 4, 1 (2017), 122–134.
[5] Chen Chen, Yi Han, Yan Chen, Hung-Quoc Lai, Feng Zhang, Beibei Wang, and K. J. Ray Liu. 2018. TR-BREATH: Time-reversal breathing rate estimation and detection. *IEEE Transactions on Biomedical Engineering* 65, 3 (2018), 489–501.
[6] Tzi-Dar Chiueh, Pei-Yun Tsai, and I-Wei Lai. 2012. *Baseband receiver design for wireless MIMO-OFDM communications*. John Wiley & Sons.

[7] Philippe De Doncker. 2003. Spatial correlation functions for fields in three-dimensional Rayleigh channels. *Progress In Electromagnetics Research* 40 (2003), 55–69.

[8] Wesley M Gifford, William Wei-Liang Li, Ying Jun Zhang, and Moe Z Win. 2011. Effect of bandwidth on the number of multipath components in realistic wireless indoor channels. In *Communications (ICC), 2011 IEEE International Conference on*. IEEE, 1–6.

[9] David A Hill. 2009. *Electromagnetic fields in cavities: deterministic and statistical theories*. Vol. 35. John Wiley & Sons.

[10] Ahmed E Kosba, Ahmed Saeed, and Moustafa Youssef. 2012. Rasid: A robust wlan device-free passive motion detection system. In *Proc. of IEEE International Conferentce on Pervasive computing and communications*. IEEE, 180–189.

[11] Oscar D Lara, Miguel A Labrador, et al. 2013. A survey on human activity recognition using wearable sensors. *IEEE Communications Surveys and Tutorials* 15, 3 (2013), 1192–1209.

[12] Jiguang Lv, Wu Yang, Liangyi Gong, Dapeng Man, and Xiaojiang Du. 2016. Robust wlan-based indoor fine-grained intrusion detection. In *Proc. of IEEE Global Communications Conference (GLOBECOM)*. IEEE, 1–6.

[13] Subhas Chandra Mukhopadhyay. 2015. Wearable sensors for human activity monitoring: A review. *IEEE sensors journal* 15, 3 (2015), 1321–1330.

[14] Qifan Pu, Sidhant Gupta, Shyamnath Gollakota, and Shwetak Patel. 2013. Whole-home Gesture Recognition Using Wireless Signals. In *Proc. of the 19th Annual International Conference on Mobile Computing & Networking*. ACM, 27–38. https://doi.org/10.1145/2500423.2500436

[15] Kun Qian, Chenshu Wu, Zheng Yang, Yunhao Liu, and Zimu Zhou. 2014. PADS: Passive Detection of Moving Targets with Dynamic Speed using PHY Layer Information. In *IEEE International Conference on Parallel and Distributed Systems*.

[16] Wenjie Ruan, Quan Z Sheng, Lei Yang, Tao Gu, Peipei Xu, and Longfei Shangguan. 2016. AudioGest: enabling fine-grained hand gesture detection by decoding echo signal. In *Proceedings of the 2016 ACM International Joint Conference on Pervasive and Ubiquitous Computing*. ACM, 474–485.

[17] Souvik Sen, Božidar Radunovic, Romit Roy Choudhury, and Tom Minka. 2012. You Are Facing the Mona Lisa: Spot Localization Using PHY Layer Information. In *Proc. of the 10th International Conference on Mobile Systems, Applications, and Services*. ACM, 183–196. https://doi.org/10.1145/2307636.2307654

[18] Ph Van Dorp and FCA Groen. 2008. Feature-based human motion parameter estimation with radar. *IET Radar, Sonar & Navigation* 2, 2 (2008), 135–145.

[19] Hao Wang, Daqing Zhang, Junyi Ma, Yasha Wang, Yuxiang Wang, Dan Wu, Tao Gu, and Bing Xie. 2016. Human respiration detection with commodity wifi devices: do user location and body orientation matter?. In *Proceedings of the 2016 ACM International Joint Conference on Pervasive and Ubiquitous Computing*. ACM, 25–36.

[20] Wei Wang, Alex X Liu, Muhammad Shahzad, Kang Ling, and Sanglu Lu. 2017. Device-free human activity recognition using commercial WiFi devices. *IEEE Journal on Selected Areas in Communications* 35, 5 (2017), 1118–1131.

[21] Xiaogang Wang. 2013. Intelligent multi-camera video surveillance: A review. *Pattern recognition letters* 34, 1 (2013), 3–19.

[22] Yan Wang, Jian Liu, Yingying Chen, Marco Gruteser, Jie Yang, and Hongbo Liu. 2014. E-eyes: Device-free Location-oriented Activity Identification Using Fine-grained WiFi Signatures. In *Proc. of the 20th Annual International Conference on Mobile Computing & Networking*. ACM, 617–628. https://doi.org/10.1145/2639108.2639143

[23] Chenshu Wu, Zheng Yang, Zimu Zhou, Xuefeng Liu, Yunhao Liu, and Jiannong Cao. 2015. Non-invasive detection of moving and stationary human with wifi. *IEEE Journal on Selected Areas in Communications* 33, 11 (2015), 2329–2342.

[24] Dan Wu, Daqing Zhang, Chenren Xu, Hao Wang, and Xiang Li. 2017. Device-Free WiFi Human Sensing: From Pattern-Based to Model-Based Approaches. *IEEE Communications Magazine* 55, 10 (2017), 91–97.

[25] Jiang Xiao, Kaishun Wu, Youwen Yi, Lu Wang, and Lionel M Ni. 2013. Pilot: Passive device-free indoor localization using channel state information. In *Proc. of IEEE International Conference on Distributed Computing Systems (ICDCS)*. IEEE, 236–245.

[26] Yaxiong Xie, Zhenjiang Li, and Mo Li. 2015. Precise power delay profiling with commodity wifi. In *Proceedings of the 21st Annual International Conference on Mobile Computing and Networking*. ACM, 53–64.

[27] Tong Xin, Bin Guo, Zhu Wang, Pei Wang, Jacqueline Chi Kei Lam, Victor Li, and Zhiwen Yu. 2018. FreeSense: A Robust Approach for Indoor Human Detection Using Wi-Fi Signals. *Proceedings of the ACM on Interactive, Mobile, Wearable and Ubiquitous Technologies* 2, 3 (2018), 143.

[28] Jaeseok Yun and Min-Hwan Song. 2014. Detecting direction of movement using pyroelectric infrared sensors. *IEEE Sensors Journal* 14, 5 (2014), 1482–1489.

[29] Dongheng Zhang, Yang Hu, Yan Chen, and Bing Zeng. 2019. BreathTrack: Tracking Indoor Human Breath Status via Commodity WiFi. *IEEE Internet of Things Journal* (2019).

[30] Feng Zhang, Chen Chen, Beibei Wang, and K. J. Ray Liu. 2018. WiSpeed: A statistical electromagnetic approach for device-free indoor speed estimation. *IEEE Internet of Things Journal* 5, 3 (2018), 2163–2177.

[31] Yang Zhao and Neal Patwari. 2015. Robust estimators for variance-based device-free localization and tracking. *IEEE Transactions on Mobile Computing* 14, 10 (2015), 2116–2129.

[32] Zimu Zhou, Zheng Yang, Chenshu Wu, Longfei Shangguan, and Yunhao Liu. 2014. Omnidirectional coverage for device-free passive human detection. *IEEE Transactions on Parallel and Distributed Systems* 25, 7 (2014), 1819–1829.
[33] Hai Zhu, Fu Xiao, Lijuan Sun, Ruchuan Wang, and Panlong Yang. 2017. R-TTWD: Robust device-free through-the-wall detection of moving human with WiFi. *IEEE Journal on Selected Areas in Communications* 35, 5 (2017), 1090–1103.
[34] Han Zou, Yuxun Zhou, Jianfei Yang, Weixi Gu, Lihua Xie, and Costas Spanos. 2017. Freedetector: Device-free occupancy detection with commodity wifi. In *Sensing, Communication and Networking (SECON Workshops), 2017 IEEE International Conference on*. IEEE, 1–5.